Row–Column Addressed Arrays for Nondestructive Evaluation Applications

James P. Kirkpatrick, Paul D. Wilcox, and Robert A. Smith

***Abstract*— Row–column addressed (RCA) arrays are 2-D arrays formed by two orthogonal overlapping linear arrays made up of elongated elements. This substantially reduces the number of elements in the 2-D array. Modeled data are used to compare RCA arrays in pulse-echo mode to fully populated 2-D arrays for nondestructive evaluation (NDE) applications and an improved beamforming algorithm based on the total focusing method is tested. Improved beamforming has led to a less than half-wavelength diameter conical bottom hole being successfully detected experimentally using an RCA array, with a maximum signal-to-noise ratio of 17.0 dB (3.s.f). The average difference between the −6-dB drop width and the nominal drill bit diameter when sizing flat bottom holes experimentally using RCA arrays is also improved compared to plane B-scan algorithms from (1.29 ± 0.07) mm to (0.23 ± 0.04) mm. These developments demonstrate the advantages of using RCA arrays over conventional fully populated 2-D arrays and provide a basis for their use, and development, in the field of NDE.**

***Index Terms*— Array signal processing, focusing, imaging, inspection, nondestructive testing, ultrasonic imaging, ultrasonic transducer arrays, ultrasonic transducers.**

I. Introduction

ROW–COLUMN addressed (RCA) arrays, also called crossed-electrode transducer arrays [1] or top orthogonal to bottom electrode arrays [2], are different from fully populated 2-D arrays in that they are effectively formed by two orthogonally orientated linear arrays with n_e transmit elements being orthogonal to n_e receive elements (Fig. 1). RCA arrays, therefore, reduce the number of interconnections, compared to a fully populated 2-D array, by a factor of $\frac{1}{2}n_e$. These reductions enable the production of 2-D arrays that would currently be impossible to manufacture while also reducing the amount of data per frame. Provided the imaging performance of RCA arrays can match that of fully populated 2-D arrays, their benefits are clear.

RCA arrays were originally invented for use in through-transmission nondestructive evaluation (NDE) in order to decrease the number of elements in 2-D arrays and increase the scanning speed [3]. In addition to continued use in through-transmission NDE [4], [5], these arrays have been used for different applications including particle manipulation [6], photoacoustic imaging [2], and medical imaging [1]. In the simplest case, image volumes can be formed by using the assumption that each A-scan originates from a fictional element located at the intersection between the physical transmit and receive elements [Fig. 1(b)] [7]. Recently, a number of developments have been made in the medical ultrasonics field because of increased interest in RCA arrays. Advances in the design of, and imaging using, RCA arrays have been well summarized in [8], which is currently the most definitive paper on RCA arrays in the medical field. Improved beamforming techniques for medical imaging are shown and a new apodization scheme was demonstrated to reduce the edge effects of elongated RCA array elements and significantly increase the imaging quality to a level comparable with fully populated 2-D arrays. Similarly, the field of NDE has made significant advances in the past 20 years with the growing use of arrays in the industry as well as the increased adoption of the total focusing method (TFM) [10]. Many of these advances have come about by the use of systematic approaches, which combine modeling and experiment. Array models are often used to predict the performance of particular arrays and test potential improvements, as well as being used to assess imaging algorithms in both medical [11] and NDE fields [12], [13].

While advances have been made in both the medical and NDE fields, the use of RCA arrays for NDE has been predominantly limited to through-transmission. However, in 2011, a commercial device which used an RCA array and operated in pulse-echo mode was produced specifically for NDE. While the device has been introduced into industry, there is a lack of literature covering the use of RCA arrays in pulse-echo mode for NDE applications. Wong *et al.* [7] attempted to use a medical RCA array to demonstrate the use of RCA arrays for NDE. This approach, however, was not representative of the state-of-the-art in NDE because of, for example, the size of the array, the use of a medical array, surface scanning, and reference subtraction. Also, results were shown using images with low dynamic range. Although the basic imaging algorithms and arrays for medical and NDE fields are similar, the requirements are often different. These differences include: the importance of signal-to-coherent and signal-to-random noise, the strength and quantity of scatterers, and the use of multiple modes. Therefore, with the additional possibility of an NDE specific RCA array, there is a need to review pulse-echo RCA array use for NDE using current state-of-the-art processes and imaging algorithms on representative samples.

The organization of this paper is as follows. First, the methodology used to obtain modeled and experimental data is introduced. Then, the data processing algorithms

Manuscript received June 4, 2018; accepted March 28, 2019. Date of publication April 3, 2019; date of current version June 5, 2019. This work was supported in part by the Engineering and Physical Sciences Research Council (EPSRC) through the U.K. Research Centre for Non-Destructive Evaluation (RCNDE) under Grant EP/L015587/1 and in part by the Defence Science and Technology Laboratory (DSTL). *(Corresponding author: James P. Kirkpatrick.)*

The authors are with the Department of Mechanical Engineering, University of Bristol, Bristol BS8 1TR, U.K. (e-mail: j.kirkpatrick@physics.org; p.wilcox@bristol.ac.uk; robert.smith@bristol.ac.uk).

Digital Object Identifier 10.1109/TUFFC.2019.2909138

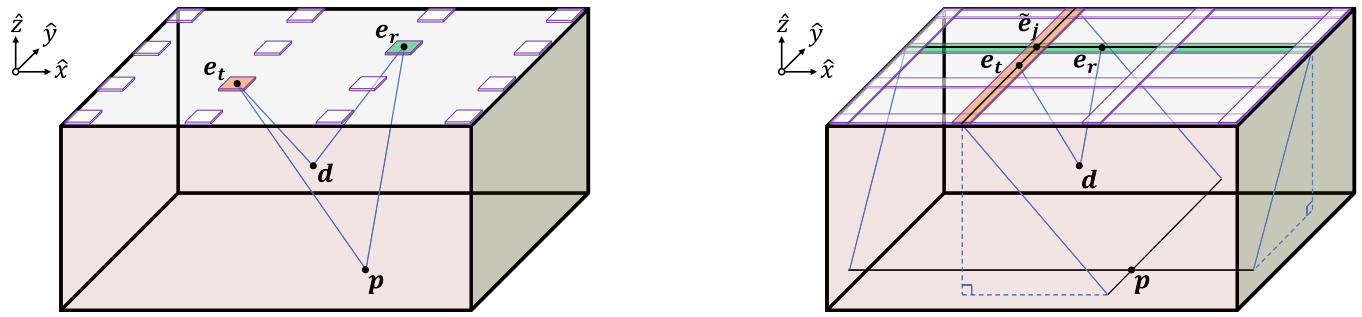

Fig. 1. Path calculation diagram for different types of 2-D array with $n_e = 4$. (a) Fully populated 2-D array and (b) RCA array. $\mathbf{e_t}$ and $\mathbf{e_r}$ are the element centers for the transmit and receive elements, respectively. $\tilde{\mathbf{e}}_j$ is the center of the fictional element used for PB1 and PB4 imaging algorithms for the RCA array. $\mathbf{d}$ and $\mathbf{p}$ are the locations of a perfect point reflector target and a voxel, respectively.

for imaging and evaluation are proposed. Modeling results are evaluated using the point spread function (PSF) in Section III-A, and experimental results are compared using the detectability and sizing of holes in acrylic in Section III-B. A discussion of the results follows in Section IV before conclusions are drawn in Section V.

II. Method

A. Modeling

A 3-D frequency-domain-linear-time-invariant model was used to calculate the frequency-domain array response, H_{tr}, as a function of frequency, f, of an array to a perfect point reflector target located at $\mathbf{d}$ in a semi-infinite homogeneous medium when transmitting and receiving on elements t and r, respectively. The equation for this approach is given by:

$$H_{tr}(f) = \Psi_0(f)\frac{1}{|\mathbf{b_t}|\,|\mathbf{b_r}|}\Gamma_t(\theta_t, \varphi_t, f)\Gamma_r(\theta_r, \varphi_r, f)\exp\left(-i2\pi f\frac{|\mathbf{b_t}| + |\mathbf{b_r}|}{v_l}\right) \quad (1)$$

where

$$\theta_j = \arccos\left(\frac{\mathbf{b_j}\cdot\hat{\mathbf{z}}}{|\mathbf{b_j}|}\right)$$
$$\varphi_j = \arctan\left(\frac{\mathbf{b_j}\cdot\hat{\mathbf{y}}}{\mathbf{b_j}\cdot\hat{\mathbf{x}}}\right)$$
$$\mathbf{b_j} = \mathbf{e_j} - \mathbf{d}$$

Ψ_0 is the input pulse frequency spectrum, Γ is the element directivity function, θ and φ are the polar and azimuthal angles between an element with its center located at $\mathbf{e}$ and the target, respectively, v_l is the longitudinal wave velocity in the medium, j represents either t or r for transmit or receive indices, respectively, and $i = (-1)^{1/2}$. The directivity functions used can be found in [14] and [15]. Beam spread and wave propagation are shown explicitly. This model is only valid in the far-field of the elements.

The length of the RCA array elements means that targets of interest are likely to be in the near field of the elements. To allow (1) to be used, the RCA array elements were modeled by dividing each element into a number of subelements for which the far-field assumption was valid. The responses for these subelements were calculated, in transmit and receive, before being summed to give the total response for each elongated element combination as shown by the following equation:

$$H_{tr}(f) = \sum_{k,m} H_{t_k r_m}(f) \quad (2)$$

where k and m are the subelement indices for transmit and receive elements, respectively. The position of the point reflector was always kept beneath the center of the array. A three-cycle Hann-weighted sine wave was used as the input pulse. For consistency with the experimental setup, acrylic was used as the medium for modeling using $v_l = 2700\,\mathrm{m\,s^{-1}}$ and a shear wave velocity of $v_s = 1100\,\mathrm{m\,s^{-1}}$. Details of the arrays used in modeling can be found in Table I.

B. Experiment

1) Experimental Array: Data were collected using an RCA array called DolphiCam (DolphiTech, Model CF08). This array first propagates ultrasound through a soft, conformable silicone-based coupling pad, which is used to make contact with the sample surface so that the array can be used with or without couplant. Details of this array can be found in Table II.

2) Sample: An acrylic test sample was manufactured in order to qualitatively validate the findings of the model. Acrylic was chosen because it closely matches the acoustic properties of carbon fiber reinforced polymer (CFRP) for which the experimental array was designed. However, unlike CFRP, acrylic is homogeneous which matches the modeling conditions. The test sample was 8 mm thick and contained a 0.3-mm-diameter conical bottom hole as well as a series of flat bottom holes with diameters of 1, 2, 4, 5, and 10 mm. These were all drilled to a depth of 3 mm, which meant that their tips were approximately 5 mm deep when measured from the front surface with the experimental array. The 0.3-mm conical bottom hole was chosen as the smallest target defect to try to resolve experimentally and is below the half-wavelength diffraction limit of ≈ 0.4 mm (1.s.f). The flat bottom holes were chosen because they have a response similar to delaminations, which are commonly sought defects for detection and sizing in CFRP.

TABLE I
MODELED ARRAY PARAMETERS

Parameter Name	Notation	Value		Unit
Array type	-	RCA	2-D	-
Centre frequency	f_0	3.5	3.5	MHz
Array width range	n_e	3-149	3-81	No. of elements
Total number of elements	N_e	$2n_e$	${n_e}^2$	-
Element pitch (half-wavelength)	ℓ_1	0.385	0.385	mm
Element width	ℓ_2	0.308	0.308	mm
Element length	ℓ_3	$\ell_1(n_e-1)+\ell_2$	0.308	mm

TABLE II
EXPERIMENTAL ARRAY PARAMETERS [16]

Parameter Name	Notation	Value	Unit
Array name	-	DolphiCam CF08	-
Centre frequency	f_0	3.5 [1]	MHz
Bandwidth $(-6\,\mathrm{dB})$	Δf	50% [1]	-
Array width	n_e	124	No. of elements
Element pitch	ℓ_1	0.250	mm
Element width	ℓ_2	0.210	mm
Element length	ℓ_3	30.96	mm
Coupling Pad			
- Thickness	ℓ_4	3	mm
- Longitudinal wave velocity	v_l	950	$\mathrm{m\,s^{-1}}$

[1] Approximate values estimated from the frequency spectrum provided.

3) Data Collection: Twelve complete and independent data sets were taken for each defect using a single-element aperture in transmit and receive. Eight software averages were taken for each A-scan using the manufacturer's software and no focusing was used when collecting data. A matched filter is used by the device by default [16] to filter the data because of the double square wave used for excitation. The raw data set was then extracted from the device and stored along with the calibration standoff values which were provided by the manufacturer. Couplant was used to improve coupling performance. Twelve complete and independent data sets were also taken from areas of the acrylic sample where no holes were located.

C. Imaging

1) General Case: Two main imaging algorithms were used for both modeled and experimental data. These were the plane B-scan and TFM algorithms, which are unfocussed and focused algorithms, respectively. The plane B-scan image, I, at a voxel located at $\mathbf{p}$, is given by the following equation:

$$I(\mathbf{p}) = \sum_{t,r} \Lambda_t \Lambda_r h_{tr}\left(\frac{\left|\mathbf{c_t}\cdot\hat{\mathbf{z}}\right| + \left|\mathbf{c_r}\cdot\hat{\mathbf{z}}\right|}{v_l}\right) \tag{3}$$

where

$$\mathbf{c_j} = \mathbf{e_j} - \mathbf{p}.$$

Λ_j is the aperture function and h_{tr} is the time-domain array response. Λ_j is given by the following equation:

$$\Lambda_j = \begin{cases} 1 & \text{if } \sqrt{(\mathbf{c_j}\cdot\hat{\mathbf{x}})^2 + (\mathbf{c_j}\cdot\hat{\mathbf{y}})^2} \le \dfrac{a}{2} \\ 0 & \text{otherwise} \end{cases} \tag{4}$$

where a is the aperture width. Plane B-scans for RCA arrays were generated using the approximation that an A-scan from any orthogonal transmit–receive combination originated from a fictional element located at the intersection of the physical elements. For example, if the elongation direction of the elements are in the $\hat{\mathbf{y}}$- and $\hat{\mathbf{x}}$-directions for transmit and receive, respectively, then the center of the fictional element would be given by $\tilde{\mathbf{e}}_j = (e_{t_x}, e_{r_y}, e_{j_z})$. Two different Plane B-scan apertures were used. These were $a = \ell_1$ and $a = 4\ell_1$ which are denoted as PB1 and PB4, respectively. PB4 was used in order to emulate the default data collection method set by the DolphiCam device which is that four elements are used in transmit in order to increase the amount of energy put into the system and, by widening the aperture, to increase the downward component of the directivity function.

Similarly, the TFM image is given by the following equation:

$$I(\mathbf{p}) = \sum_{t,r} \Upsilon_t \Upsilon_r h_{tr}\left(\frac{|\mathbf{c_t}| + |\mathbf{c_r}|}{v_l}\right) \tag{5}$$

where Υ_j is the angle limit function given by the following equation:

$$\Upsilon_j = \begin{cases} 1 & \arccos\left(\dfrac{\mathbf{c_j}\cdot\hat{\mathbf{z}}}{|\mathbf{c_j}|}\right) \le \theta_{\text{limit}} \\ 0 & \text{otherwise} \end{cases} \tag{6}$$

and θ_{limit} is the angle limit at the pixel. The RCA-adapted TFM algorithm uses the shortest time path between the center line of an element and a voxel in both transmit and receive. This algorithm is preferable for NDE compared to the proposed medical algorithm suggested in [8] and [9] because there is no defocussing in postprocessing. However, this is at the cost of a lower input energy leading to a decrease in signal to random noise ratio.

One final step was added to all algorithms used, which was to divide the amplitude of every voxel by the number of transmit–receive combinations which contribute to the voxel. This is especially important when there is a combination of angle limiting and a large amount of refraction because the range of contributions per voxel is large. This division by the number of contributions helps to normalize the response from reflectors at different locations. Without it, responses from a reflector at each voxel would vary considerably in amplitude.

When imaging the experimental data, a broadband frequency-domain Gaussian filter with $\Delta f \approx 150\%$ was applied to the raw A-scans before imaging. It was also

assumed, for simplicity, that the array was parallel to the interface between the coupling pad and the sample in all directions. In line with this assumption, a single value for the thickness of the coupling pad, averaged across the whole array, was calculated using the highest amplitude reflection within the first 50 time points for each A-scan. This coupling pad thickness was used in all the path calculations. Modifications were made to the RCA-adapted TFM algorithm because of refraction due to the interface between the coupling pad and the sample. The interface was discretized and the shortest time path was calculated by finding the shortest time path for each element to interface point to voxel combination in 2-D. Apart from modifications relating to the coupling pad, data from the DolphiCam device were processed using the imaging algorithms described in (3) and (5). An angle limit of $\theta_{\text{limit}} = 30°$ was used during all experimental implementations of the RCA-adapted TFM algorithm. The imaging algorithms were also applied to the data sets taken on areas of the sample which did not contain holes. These images were used to quantify the root-mean-squared (RMS) noise.

2) Simplification and Computational Efficiency: On a regular Cartesian imaging grid, symmetry reduces (5) for RCA arrays to two 2-D path calculations, one in transmit and one in receive, which improves the speed of the algorithm. Both are calculated using (5) in 2-D as if there were two linear arrays perpendicular in orientation with one in transmit and one in receive. For example, if the elongation direction of the elements are in the $\hat{\mathbf{y}}$- and $\hat{\mathbf{x}}$-directions for transmit and receive, respectively, the transmit path calculation would be calculated in the $\hat{\mathbf{y}}$ plane (the plane for which $\hat{\mathbf{y}}$ is the normal) and the receive path calculation in the $\hat{\mathbf{x}}$ plane, as shown schematically in Fig. 1(b). Here, $n_{e_t} = n_{e_r}$ and $n_{p_x} = n_{p_y}$ symmetry simplifies the problem further and improves the speed of the algorithm. In this case, only $n_{e_t} \times n_{p_x} \times n_{p_z}$ paths need to be calculated. This is substantially less than the number of calculations required for full 3-D path calculations for every element for fully populated 2-D arrays using the TFM algorithm.

D. Evaluation

1) Point Spread Function Evaluation: The PSF was calculated for both types of array and all imaging algorithms considered by applying the imaging algorithms to the modeled data. The PSF was used to compare the imaging performance of both fully populated 2-D arrays and RCA arrays and their respective imaging algorithms. A decibel scale, normalized to the maximum amplitude of the PSF, was used. The imaging performance was quantified using a measurement of the -6-dB drop volume of the PSF, $V_{-6\,\text{dB}}$, which was calculated by summing the number of voxels with an amplitude greater than $-6\,\text{dB}$ and multiplying it by the volume of one voxel, V_p. The uncertainty in this value, $\alpha_{V_{-6\,\text{dB}}}$, was estimated using the maximum uncertainty in the volume of a sphere placed in a regular 3-D Cartesian grid, which was calculated using the relationship between the surface area and volume of a sphere, yielding an uncertainty of $\alpha_{V_{-6\,\text{dB}}} = ((9/2)\pi V_p V_{-6\,\text{dB}}^2)^{(1/3)}$.

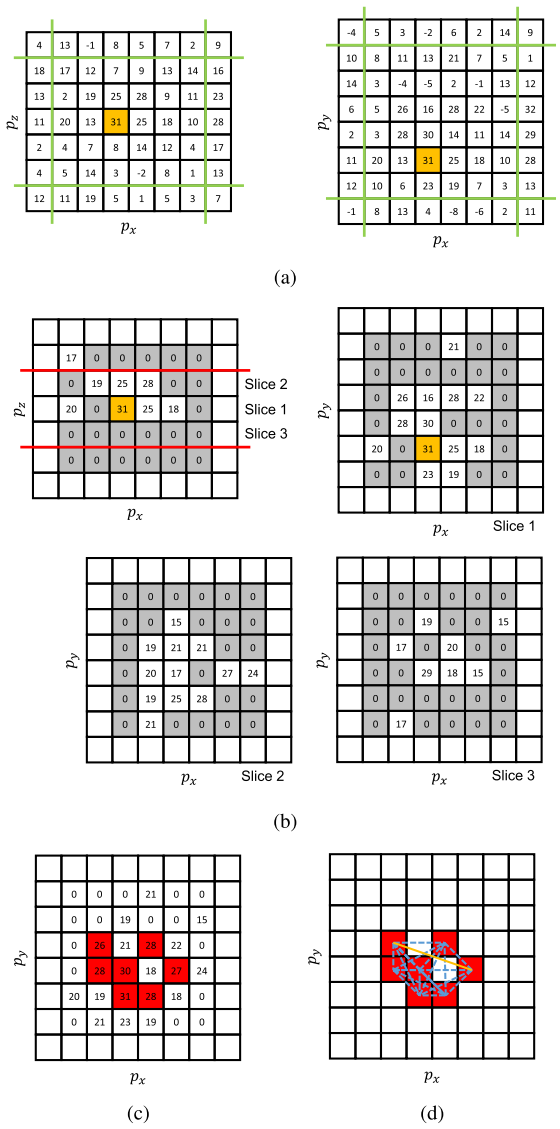

Fig. 2. Automated procedure used to size the flat bottom holes. (a) Maximum amplitude within the region of interest was located. (b) All amplitudes below the 15-dB detectability threshold were then disregarded by setting them to zero and all voxels that satisfied the condition $\left|(\mathbf{p} - \mathbf{p}_{\text{max}}) \cdot \hat{\mathbf{z}}\right| \leq 0.05$ mm were selected. (c) Amplitudes of these voxels at each (p_x, p_y) location were condensed into a single amplitude by taking the maximum and all locations with an amplitude greater than 6 dB below the maximum amplitude were selected. (d) -6-dB drop width was given by the maximum distance between any two of these locations.

2) Detectability and Sizing: The data sets that were taken on areas of the sample where no holes were located were imaged using the imaging algorithms described earlier. The RMS of the image voxels in the range $(-6\,\text{mm} \leq p_z \leq -4\,\text{mm})$ was calculated for each data set and for each imaging algorithm. This range was selected in order to calculate the rms noise value around the defect location ($p_z \approx -5\,\text{mm}$). The mean of the 12 data sets was taken to give a single RMS noise value for each imaging algorithm. An arbitrary conservative detectability threshold of 15 dB above the rms noise level was set for successful detection of a defect. Following detection, the flat bottom holes were sized using the following automated procedure (Fig. 2). First, the location of the maximum amplitude in the image, $\mathbf{p}_{\text{max}}$, was located within the region

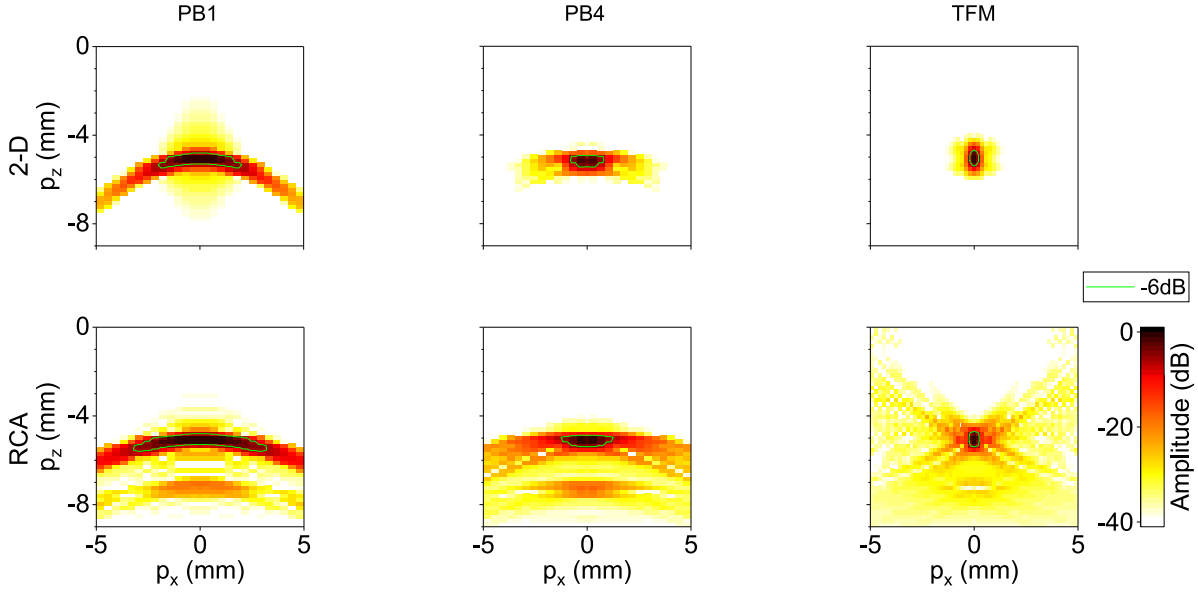

Fig. 3. B-scan images at $p_y = 0$ mm of the PSF with a target at $\mathbf{d} = (0, 0, -5)$ mm for $n_e = 41$ from modeled data. Fully populated 2-D and RCA arrays are shown from top to bottom, respectively. PB1, PB4, and TFM imaging algorithms are shown from left to right, respectively.

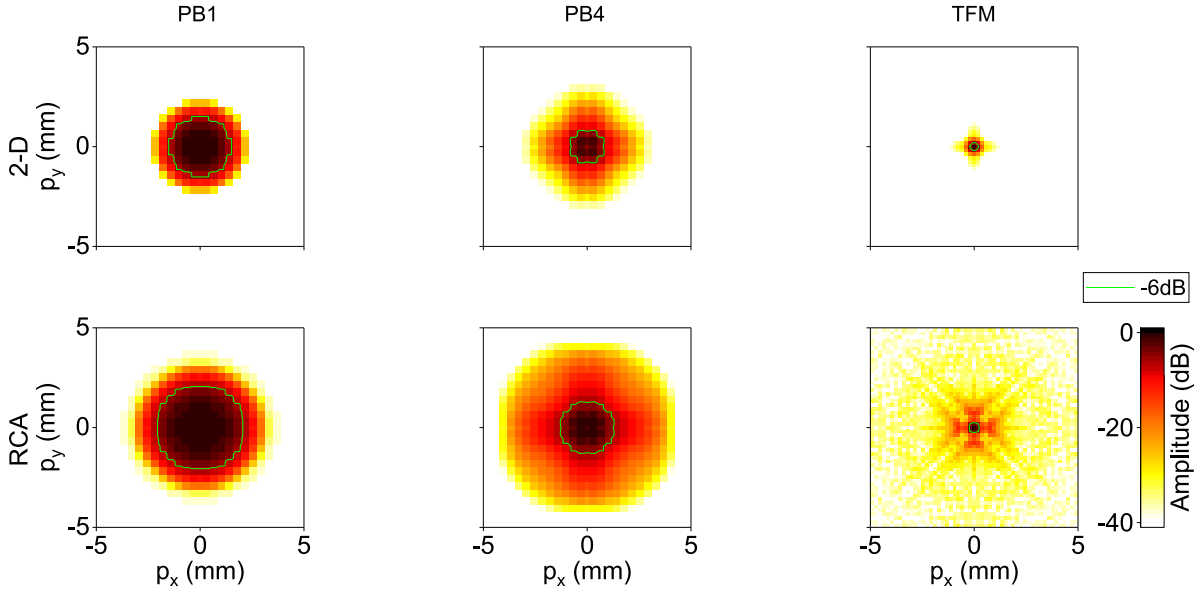

Fig. 4. C-scan images at $p_z = -5$ mm of the PSF with a target at $\mathbf{d} = (0, 0, -5)$ mm for $n_e = 41$ from modeled data. Fully populated 2-D and RCA arrays are shown from top to bottom, respectively. PB1, PB4, and TFM imaging algorithms are shown from left to right, respectively.

of interest [Fig. 2(a)]. The region of interest was selected to be (-13 mm $\leq p_x \leq$ 13 mm), (-13 mm $\leq p_y \leq$ 13 mm), and (-6 mm $\leq p_z \leq -4$ mm). All amplitudes below 15 dB were then disregarded by setting them to zero because the confidence that they originate from a defect is low. All voxels within the region of interest that satisfied the condition $|(\mathbf{p} - \mathbf{p}_{\max}) \cdot \hat{\mathbf{z}}| \leq 0.05$ mm were selected in order to take account of any small deviation in surface height or orientation of the flat bottom hole [Fig. 2(b)]. The amplitudes of these voxels for different p_z at each (p_x, p_y) location were condensed into a single amplitude by taking the maximum [Fig. 2(c)]. Following this, all locations with an amplitude greater than 6 dB below the maximum amplitude were stored [Fig. 2(c)]. Finally, the -6-dB drop width was given by the maximum distance between any two of these locations [Fig. 2(d)]. This process was repeated for all 12 data sets of each defect. The mean was used to give a best estimate of the -6-dB drop width and the standard error was used to quantify the uncertainty.

III. Results

A. Modeling

Example PSF B- and C-scan images for a target at $\mathbf{d} = (0, 0, -5)$ mm for the $n_e = 41$ case for both types of array and all imaging algorithms considered are shown in Figs. 3 and 4, respectively. The images are shown using a decibel scale which is normalized to the maximum amplitude of the PSF and has a 40-dB dynamic range. The PSF was calculated for a target

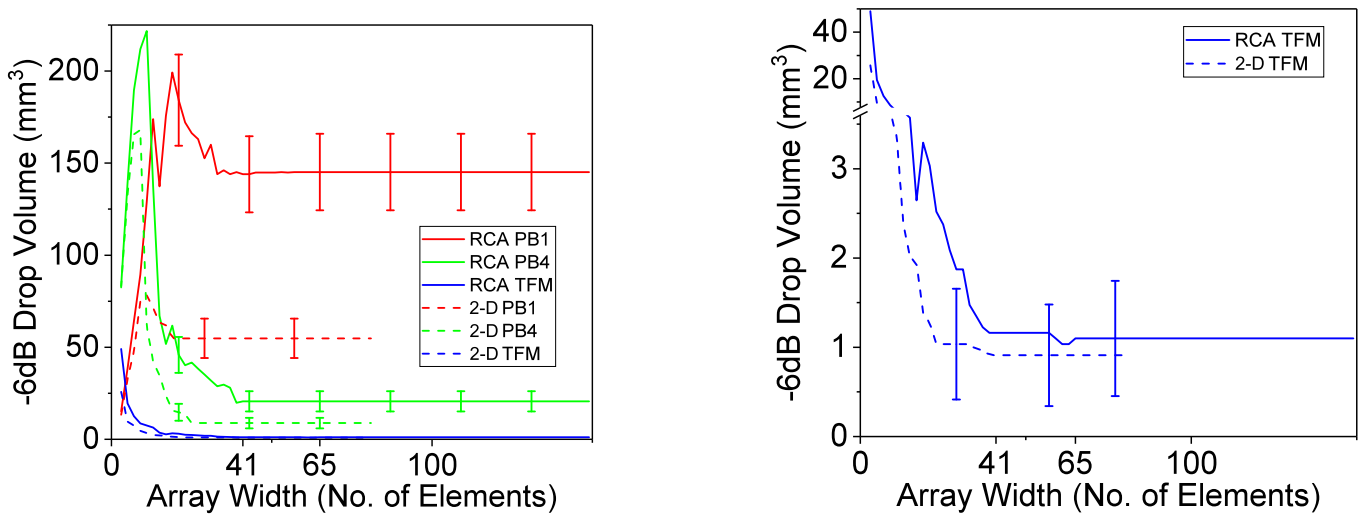

Fig. 5. −6-dB drop volume of the PSF at $\mathbf{d} = (0, 0, -5)$ mm as a function of n_e from modeled data for (a) all imaging algorithms and arrays and (b) TFM-based imaging algorithms only. A reduced number of error bars are shown for clarity.

at $\mathbf{d} = (0, 0, -5)$ mm as a function of n_e for both types of array and all imaging algorithms considered. $V_{-6\,\mathrm{dB}}$ as a function of n_e is shown in Fig. 5.

B. Experiment

The responses of the DolphiCam array to holes located at a depth of approximately 5 mm in acrylic were measured and imaged for all imaging algorithms considered. Example B- and C-scan images for every hole considered are shown in Figs. 6 and 7, respectively. The images are shown using a decibel scale which is normalized to the amplitude of the RMS noise and has a 40-dB dynamic range. The maximum value on the scale is equal to the maximum amplitude within the range ($-6\,\mathrm{mm} \leq p_z \leq -4\,\mathrm{mm}$). Finally, the DolphiCam array responses, imaged using all imaging algorithms considered, were used to size the diameters of the flat bottom holes. The −6-dB drop widths of the flat bottom holes are compared to the drill bit diameter used to make them in Fig. 8. The average difference between the −6-dB drop width and the nominal drill bit diameter across the whole range of flat bottom holes was (1.6 ± 0.1) mm, (1.29 ± 0.07) mm, and (0.23 ± 0.04) mm for PB1, PB4, and TFM imaging algorithms, respectively.

IV. Discussion

A. Point Spread Function Evaluation

It is shown from the results in Figs. 3 and 4 that fully populated 2-D arrays provide a tighter PSF than RCA arrays. For a given n_e, $V_{-6\,\mathrm{dB}}$ is shown to be smaller for fully populated 2-D arrays in all cases [Fig. 5(a)]. It can be clearly seen that the TFM-based imaging algorithms have a narrower PSF and $V_{-6\,\mathrm{dB}}$ than the PB1 and PB4 algorithms in all cases. This is as expected because the PB1 and PB4 algorithms are both unfocussed, whereas the TFM-based imaging algorithms are focused. For low values of n_e, where the PSF extends outside of the array aperture, the division of the amplitude by the number of transmit–receive combinations which contribute to a voxel causes $V_{-6\,\mathrm{dB}}$ to be artificially enlarged. At larger values of n_e, where the PSF is beneath the array, the results become stable.

It is shown in Fig. 5(b) that the TFM algorithms for the fully populated 2-D array and the RCA array quickly become within error of each other after this point. From $n_e = 65$, the difference in $V_{-6\,\mathrm{dB}}$ is only (0.2 ± 0.9) mm^3. In terms of $V_{-6\,\mathrm{dB}}$, the TFM imaging performance of the fully populated 2-D array and the RCA array can be considered comparable after this point. However, it can be seen from Figs. 3 and 4 that, outside $V_{-6\,\mathrm{dB}}$, the PSF for the RCA array is extended in all directions compared to the fully populated 2-D array. This is expected to result in a decrease in signal-to-noise ratio (SNR) [17], and therefore detectability, when using RCA arrays as opposed to fully populated 2-D arrays experimentally. This is because of the defocussing in one direction in both transmit and receive.

It has also been shown that the PB4 algorithm produced a smaller $V_{-6\,\mathrm{dB}}$ compared to the PB1 algorithm. This was in agreement with the prediction that, due to the increase in aperture size, the directivity function is narrower. The limit reached by the PB1 and PB4 algorithms in Fig. 5(a) is because, once the $V_{-6\,\mathrm{dB}}$ is beneath the array, any elements added to the side of the array do not contribute to $V_{-6\,\mathrm{dB}}$. For the TFM-style algorithms, $V_{-6\,\mathrm{dB}}$ continues to decrease as more elements are added but tends toward a limit as additional elements contribute less and less to the $V_{-6\,\mathrm{dB}}$ due to both directivity and beam spread.

B. Detectability

The SNR for the smallest hole considered, the 0.3 mm conical bottom hole, was improved using the RCA-adapted TFM algorithm. This improvement led to the response being above the 15-dB detectability threshold, while the next highest response, using the PB4 algorithm, was below the threshold

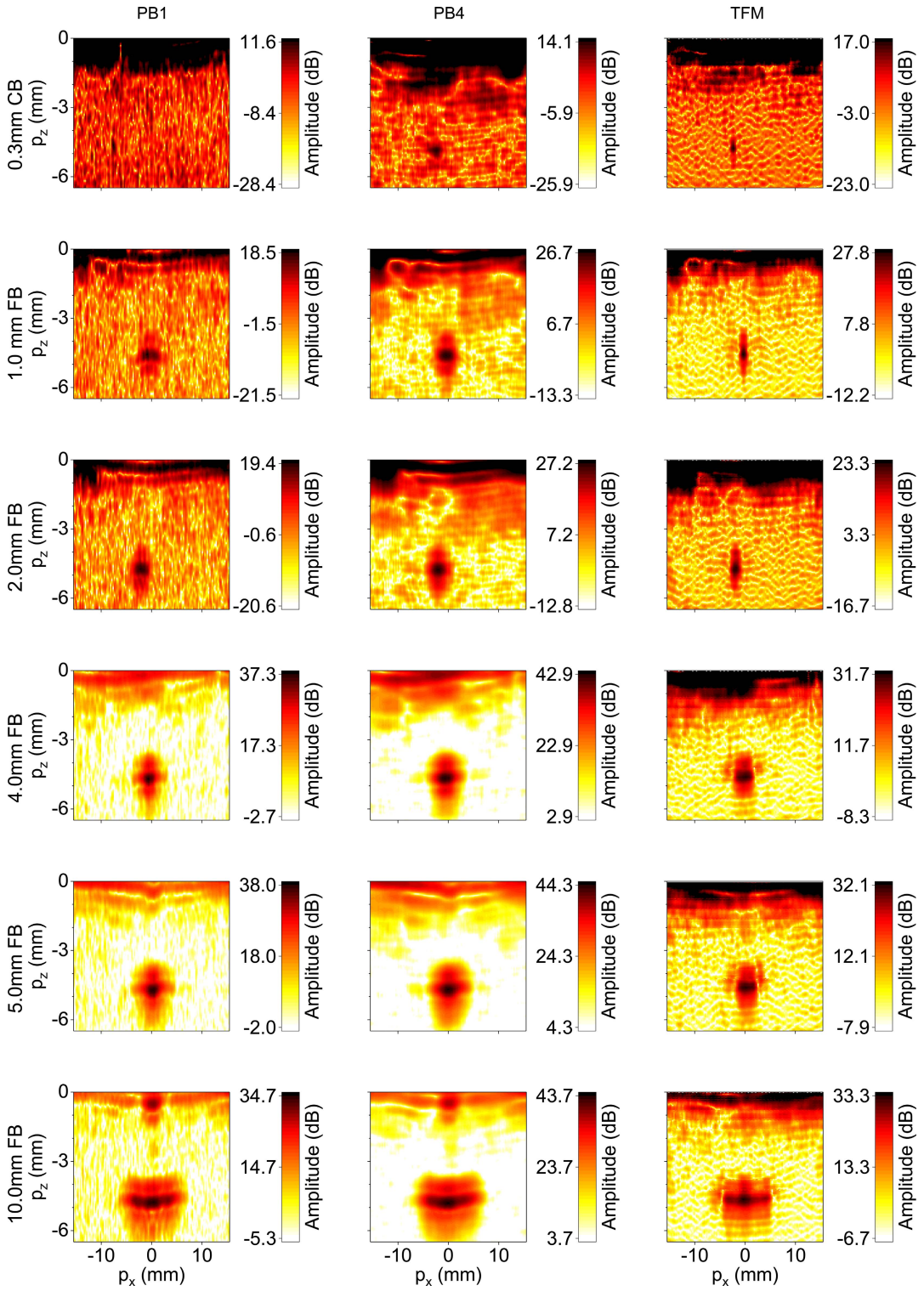

Fig. 6. B-scan images of a range of holes in acrylic at a depth of approximately −5 mm from experimental data. Increasing defect diameters are shown from top to bottom. CB and FB denote conical bottom and flat bottom, respectively. PB1, PB4, and TFM imaging algorithms are shown from left to right, respectively.

[Figs. 6 and 7]. All of the flat bottom holes considered were above the detectability threshold.

The SNR benefits of the RCA-adapted TFM algorithm also decrease as the hole diameter increases. This is expected to be because the orientation of the flat bottom holes is parallel to the sample surface and so the PB1 and PB4 algorithms are aligned to the high-amplitude specular reflection from the flat bottom hole. The RCA-adapted TFM algorithm uses a much larger set of A-scans that contain, in addition, many other signals which contribute very little apart from noise.

The responses from the holes in Figs. 6 and 7 do not show the sidelobes seen in Figs. 3 and 4 for the PB1 and

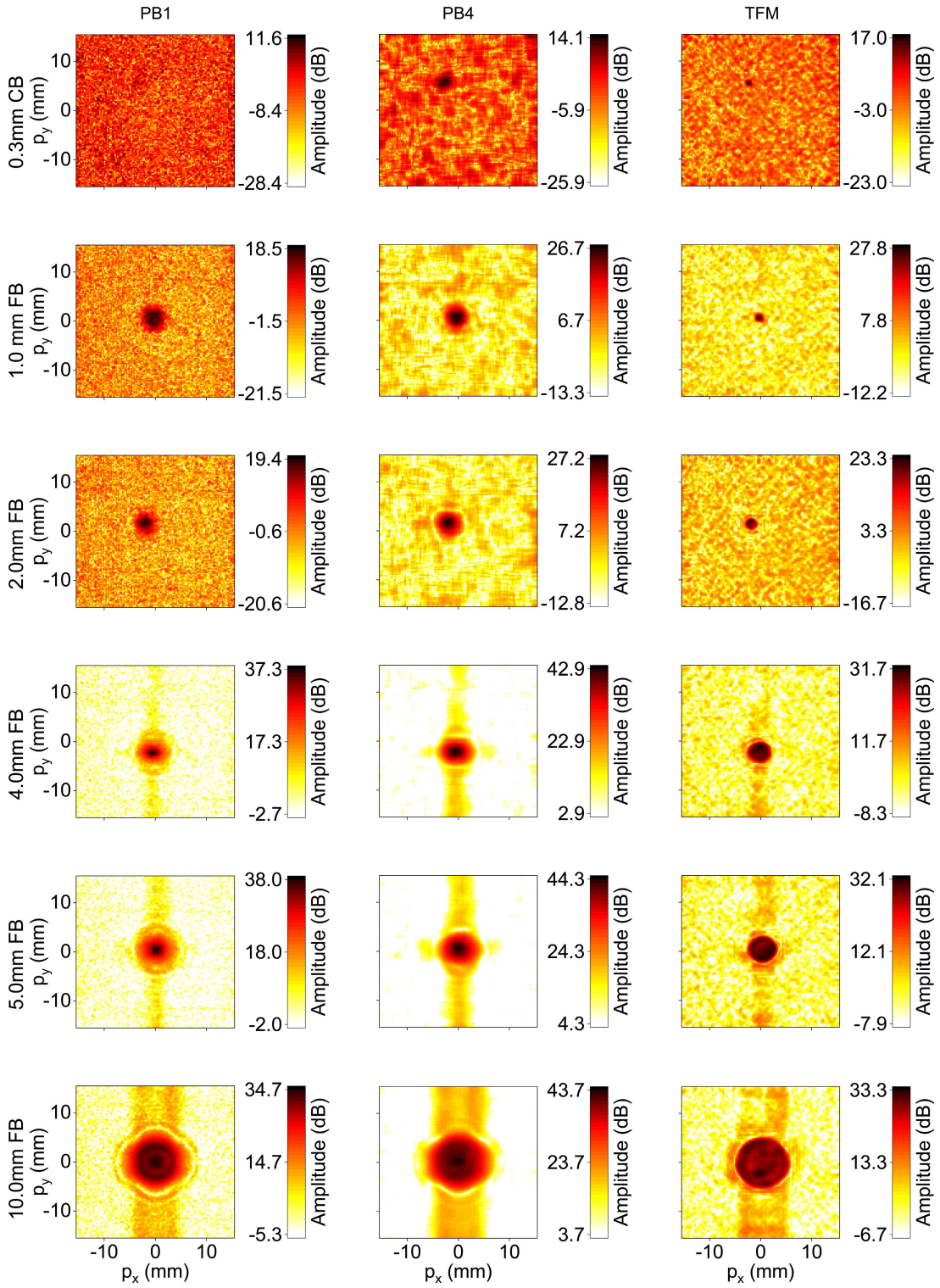

Fig. 7. C-scan images of a range of holes in acrylic at a depth of approximately −5 mm from experimental data. Increasing defect diameters are shown from top to bottom. CB and FB denote conical bottom and flat bottom, respectively. PB1, PB4, and TFM imaging algorithms are shown from left to right, respectively.

PB4 algorithms. This is because of the refraction at the interface between the coupling pad and the sample. At this interface, the critical angle $\theta_{\text{crit.}} \approx 20.6^\circ$ (3.s.f) for longitudinal waves. Therefore, the coupling pad not only stops the edge waves propagating into the sample below the center of the array but also increases the applicability of the intersection approximation used for the PB1 and PB4 algorithms by narrowing the directivity function in terms of the waves propagating into the sample. The coupling pad also reduces the benefits of a broad directivity function used by the RCA-adapted TFM

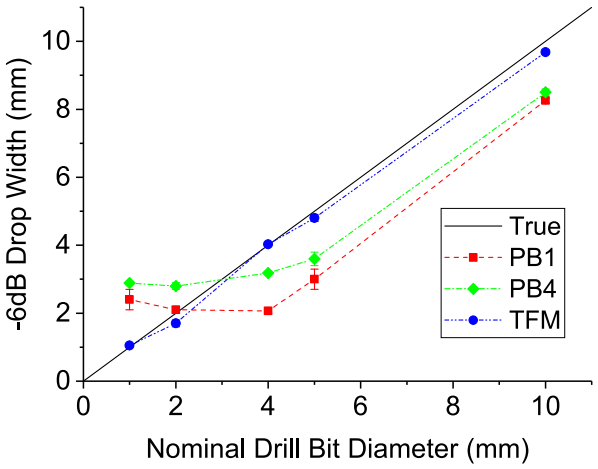

Fig. 8. Sizing of flat bottom holes in acrylic experimentally using the DolphiCam array.

algorithm. In the absence of a coupling pad, the literature shows that sidelobes have been successfully reduced using element apodization outside the main array area [8] and [9]. This would allow the use of the broad directivity function of the elements to be maximized for the RCA-adapted TFM algorithm.

The extension of the response, in terms of depth, from the holes seen for all algorithms in Fig. 6 is caused by the long length in time of the transmission pulse, which is approximately five cycles. The extension of the response, in terms of width in the p_y direction, from the 4-, 5-, and 10-mm-diameter holes seen in all algorithms in Fig. 7 is caused by the transducer design asymmetry, i.e., each set of electrodes above and below the piezoelectric material are orthogonal.

C. Sizing

Finally, the accuracy and precision of sizing flat bottom holes in acrylic have been improved by using the RCA-adapted TFM algorithm. The average difference across the whole range of hole diameters has been improved by a factor of 5.61 (3.s.f). Fig. 8 shows that the RCA-adapted TFM algorithm consistently performs better than the PB1 and PB4 algorithms across the full range of hole diameters.

The systematic error in the −6-dB drop width for the PB1 and PB4 algorithms toward the higher diameters of holes is caused by the beam profile not being circular for the RCA array. The PB1 and PB4 algorithms behave as expected toward the lower diameters of holes as they reach a sizing limit roughly proportional to their beam size [18]. Accurate values of beam size are difficult to calculate because of the refraction at the coupling pad.

The sizing limit for the RCA-adapted TFM algorithm was not reached and so cannot be conclusively stated in this paper. However, it cannot be below the half-wavelength diffraction limit.

V. Conclusion

The imaging performance of fully populated 2-D and RCA arrays was compared using frequency-domain modeling techniques. Three different imaging algorithms were applied to the modeled data in order to obtain the PSF. These consisted of two plane B-scan algorithms, with apertures of $a = \ell_1$ and $a = 4\ell_1$, and TFM algorithms. An RCA-adapted TFM algorithm was proposed in order to take account of the geometry of RCA arrays. The −6-dB drop volume of the PSF was used as the comparison metric to compare the imaging performance. For a given n_e, RCA arrays were found to perform worse than fully populated 2-D arrays for imaging in all cases. However, the imaging performance of RCA arrays was comparable to that of fully populated 2-D arrays when using the RCA-adapted TFM algorithm. The imaging performance of RCA arrays was compared experimentally for the same three imaging algorithms. The RCA-adapted TFM algorithm was shown experimentally to improve the imaging performance with respect to the detectability of a very small defect. The RCA-adapted TFM algorithm also improved the accuracy and precision of sizing flat bottom holes. The proposed RCA-adapted TFM algorithm for NDE applications shows that RCA array imaging performance can be comparable to that of fully populated 2-D arrays. This means that the improvements provided by RCA arrays in terms of data volumes, numbers of connections, and image-construction times can be fully utilized in the field of NDE. It is recommended that further work is done to develop an RCA array without a coupling pad which uses apodized elements in order to maximize the benefits of the RCA-adapted TFM algorithm and minimize energy losses caused by the coupling pad.

Acknowledgment

The authors would like to thank DolphiTech, especially E. Skoglund, F. Lingvall, and Y. Raudberget, for providing crucial information about the DolphiCam device, S. Iles for his advice and skill in manufacturing the sample, and D. Hallam for his help and support during the project. All data used in this paper are openly available for download from the University of Bristol data repository at https://doi.org/10.5523/bris.375rfm9pip3rj2wnd22fncnxvk.

References

[1] C. Morton and G. R. Lockwood, "Theoretical assessment of a crossed electrode 2-D array for 3-D imaging," in *Proc. IEEE Symp. Ultrasonics*, Oct. 2003, pp. 968–971. [Online]. Available: http://ieeexplore.ieee.org/document/1293560/

[2] R. J. Zemp, R. Chee, A. Sampaleanu, D. Rishi, and A. Forbrich, "S-sequence bias-encoded photoacoustic imaging with top orthogonal to bottom electrode (TOBE) CMUT arrays," in *Proc. IEEE Int. Ultrason. Symp.*, Jul. 2013, pp. 1197–1200.

[3] G. Curtis and A. B. Joinson, "Polyscan—A rapid, ultrasonic, through-transmission C-scanning system," in *Proc. 8th World Conf. Nondestruct. Testing*, Cannes, France, Sep. 1976, p. 8.

[4] M. Bernard, "Crossed-transducers array for transmission ultrasonic imaging," in *Proc. Ultrason. Symp.*, Oct/Nov. 1983, pp. 732–735. [Online]. Available: https://ieeexplore.ieee.org/document/1535095

[5] A. Koch, S. Gruber, T. Scharrer, K. T. Fendt, R. Lerch, and H. Ermert, "2D transmission imaging with a crossed-array configuration for defect detection," in *Proc. IEEE Int. Ultrason. Symp.*, Oct. 2012, pp. 36–39.

[6] H. Wang, Y. Qiu, C. E. M. Démoré, S. Gebhardt, and S. Cochran, "2-D crossed-electrode transducer arrays for ultrasonic particle manipulation," in *Proc. IEEE Int. Ultrason. Symp.*, Sep. 2016, pp. 1–4.

[7] L. L. P. Wong, A. I. H. Chen, Z. Li, A. S. Logan, and J. T. W. Yeow, "A row–column addressed micromachined ultrasonic transducer array for surface scanning applications," *Ultrasonics*, vol. 54, no. 8, pp. 2072–2080, Dec. 2014. doi: 10.1016/j.ultras.2014.07.002.
[8] M. F. Rasmussen, T. L. Christiansen, E. V. Thomsen, and J. A. Jensen, "3-D imaging using row-column-addressed arrays with integrated apodization—Part I: Apodization design and line element beamforming," *IEEE Trans. Ultrason., Ferroelectr., Freq. Control*, vol. 62, no. 5, pp. 947–958, May 2015.
[9] T. L. Christiansen, M. F. Rasmussen, J. P. Bagge, L. N. Moesner, J. A. Jensen, and E. V. Thomsen, "3-D imaging using row–column-addressed arrays with integrated apodization—Part II: Transducer fabrication and experimental results," *IEEE Trans. Ultrason., Ferroelectr., Freq. Control*, vol. 62, no. 5, pp. 959–971, May 2015.
[10] C. Holmes, B. W. Drinkwater, and P. D. Wilcox, "Post-processing of the full matrix of ultrasonic transmit-receive array data for non-destructive evaluation," *NDT & E Int.*, vol. 38, no. 8, pp. 701–711, Dec. 2005. doi: 10.1016/j.ndteint.2005.04.002.
[11] C. E. M. Demore, A. W. Joyce, K. Wall, and G. R. Lockwood, "Real-time volume imaging using a crossed electrode array," *IEEE Trans. Ultrason., Ferroelectr., Freq. Control*, vol. 56, no. 6, pp. 1252–1261, Jun. 2009.
[12] B. W. Drinkwater and P. D. Wilcox, "Ultrasonic arrays for non-destructive evaluation: A review," *NDT & E Int.*, vol. 39, no. 7, pp. 525–541, Oct. 2006.
[13] J. Zhang, B. W. Drinkwater, P. D. Wilcox, and A. J. Hunter, "Defect detection using ultrasonic arrays: The multi-mode total focusing method," *NDT & E Int.*, vol. 43, no. 2, pp. 123–133, Mar. 2010. doi: 10.1016/j.ndteint.2009.10.001.
[14] S.-C. Wooh and Y. Shi, "Three-dimensional beam directivity of phase-steered ultrasound," *J. Acoust. Soc. Amer.*, vol. 105, no. 6, pp. 3275–3282, Jun. 1999. doi: 10.1121/1.424655.
[15] G. F. Miller and H. Pursey, "The field and radiation impedance of mechanical radiators on the free surface of a semi-infinite isotropic solid," *Proc. Roy. Soc. London A, Math. Phys. Eng. Sci.*, vol. 223, no. 1155, pp. 521–541, May 1954.
[16] F. Lingvall and E. Skoglund, *DolphiCam 1.3 Technical Paper*. DolphiTech, 2015.
[17] P. D. Wilcox, "Array imaging of noisy materials," *AIP Conf.*, vol. 1335, no. 1 pp. 890–897, Jun. 2011.
[18] R. A. Smith, "Ultrasonic defect sizing in carbon-fibre composites: An initial study," *Insight*, vol. 36, no. 8, pp. 595–605, 1994.

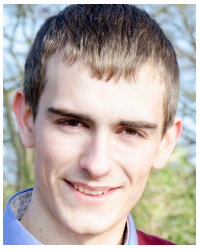

James P. Kirkpatrick was born in the U.K. He received the B.Sc. degree (Hons.) in physics from the University of Warwick, Coventry, U.K., in 2015. He is currently pursuing the Eng.D. degree with the University of Bristol, Bristol, U.K., and also with the Defence Science and Technology Laboratory, Salisbury, U.K.

His research interests include novel array transducer designs, laser ultrasonics, and ultrasonic diffuse fields.

Paul D. Wilcox was born in Nottingham, U.K., in 1971. He received the M.Eng. degree in engineering science from the University of Oxford, Oxford, U.K., in 1994 and the Ph.D. degree from Imperial College London, London, U.K., in 1998.

He remained in the Non-Destructive Testing (NDT) Research Group, Imperial College London, as a Research Associate until 2002, working on the development of guided wave array transducers for large area inspection. Since 2002, he has been with the Department of Mechanical Engineering, University of Bristol, Bristol, U.K., where his current title is Professor of dynamics. He held an EPSRC Advanced Research Fellowship in quantitative structural health monitoring from 2007 to 2012 and was Head of the Mechanical Engineering Department, University of Bristol, from 2015 to 2018. In 2015, he was a Co-Founder of Inductosense Ltd., Bristol, a spin-out company which is commercializing inductively coupled embedded ultrasonic sensors. His research interests include array transducers, embedded sensors, ultrasonic particle manipulation, long-range guided wave inspection, structural health monitoring, elastodynamic scattering, and signal processing.

Robert A. Smith received the B.A. degree in physics from the University of Cambridge, Cambridge, U.K., in 1983, the M.Sc. degree applied acoustics from the Kings College, London, U.K., in 1986, and the Ph.D. degree from the University of Nottingham, Nottingham, U.K., in 2010, with a focus on the ultrasonic 3-D characterization of fiber-reinforced composites.

He is currently a Professor of nondestructive testing (NDT) and high value manufacturing with the University of Bristol, Bristol, U.K. He spent six years at the National Physical Laboratory and then moved to the Non-Destructive Evaluation (NDE) Group, Royal Aerospace Establishment (RAE), Farnborough, U.K., in 1989. After several years as the Fellow in NDE at RAE, the Defence Evaluation and Research Agency (DERA), Farnborough, U.K., and then QinetiQ Ltd., Farnborough, he became a QinetiQ Senior Fellow in 2011. He moved to the University of Bristol in 2013 to accept a personal chair and commence a five-year EPSRC Fellowship in manufacturing. In 2018, he became the Director of the U.K. Research Centre for Non-Destructive Evaluation (RCNDE). He has authored more than 120 publications, for which he was awarded the John Grimwade Medal five times and the Roy Sharpe Prize for 1996 by the British Institute of NDT, of which he is an Honorary Fellow and was the President from 2015 to 2016. He is also a fellow of the Institute of Physics, a Chartered Physicist, and a Chartered Engineer.